Synthesis and characterisation of P-Doped Sr2MnFeO6- Systems

James, Matthew; Berry, Frank; marco, jF; Slater, Peter

DOI:
10.1149/10301.2185ecst

Document Version
Peer reviewed version

Citation for published version (Harvard):
James, M, Berry, F, marco, JF & Slater, P 2021, 'Synthesis and characterisation of P-Doped Sr_2MnFeO_{6-} Systems', *ECS Transactions*, vol. 103, no. 1, pp. 2185-2194. https://doi.org/10.1149/10301.2185ecst

Synthesis and characterisation of P-Doped $Sr_2MnFeO_{6-\delta}$ Systems

M.S. James[a], F. J. Berry[a], J. F. Marco[b], and P. R. Slater[a*]
[a] School of Chemistry, University of Birmingham, Birmingham, United Kingdom, B15 2TT
[b] Instituto de Química Física "Rocasolano", CSIC, Serrano, 119, Madrid 28006, Spain

Perovskite systems have attracted considerable interest for fuel cell/electrolyser applications. Here we show that phosphate can be incorporated into the mixed Mn/Fe system $Sr_2MnFeO_{6-\delta}$. In all cases, the conductivity was shown to increase for low doping levels (≤10 % phosphate incorporation) with a subsequent decrease for higher doping levels, attributed to the presence of $Sr_3(PO_4)_2$ impurity as the solubility limit is exceeded. The work further illustrates that phosphate can be doped into perovskite systems, highlighting this doping approach as an alternative strategy to modify the structure and properties.

Introduction

Materials with the perovskite structure have been intensively researched as novel electrode materials for Solid Oxide Fuel Cells and Electrolysers (SOFC's/SOE's). This is due to their high electronic and ionic conductivity (1-4). Traditionally, doping strategies have focused on the substitution at the A-site and/or B-site cation by aliovalent cations of a similar size, e.g. Sr for La, and Fe for Co, within $La_{1-x}Sr_xCo_{1-y}Fe_yO_{3-\delta}$ (LSCF) (5-9). However, an alternative strategy has become more prominent in recent years; doping with much smaller cations, B^{3+}, C^{4+}, Si^{4+}, P^{5+} and S^{6+}, which are accommodated as oxyanion groups (Borate, Carbonate, Silicate, Phosphate, and Sulphate) (10). This research originally stemmed from previous work on superconducting perovskite cuprates, where the successful incorporation of oxyanions was demonstrated (11-14). Studies illustrated that these perovskite-type materials showed a great propensity to accommodate oxyanions (e.g. 50% of the B sites substituted by C (as carbonate) within $Sr_2CuO_2CO_3$) and, as such, resulted in the synthesis of novel materials which would not have been possible without this doping strategy. For example, low levels of $(PO_4)^{3-}$ were incorporated within $YSr_2Cu_3O_7$, which cannot not be prepared undoped, resulting in the formation of the new phase, $YSr_2Cu_{2.79}(PO_4)_{0.21}O_{6.16}$ (15).

More recently, oxyanion doping strategies, in particular phosphate, have been studied in more detail for their potential use in SOFC/SOE as well as Alkaline Fuel Cell (AFC) applications (16-22). Due to the high temperatures necessary to prepare and operate the SOFC/SOE cells, oxyanions with a high thermal stability are required in these applications. Therefore, initial work has focused on phosphate (as well as sulphate) doping (23-24). Previous work has shown that the incorporation of phosphate within $SrCoO_{3-\delta}$ stabilises a cubic perovskite structure, which allows for a substantial increase in conductivity compared to the undoped variant with a hexagonal perovskite structure (25). Phosphate doping has also been extended to $CaMnO_{3-\delta}$ and the doping strategy was also shown to improve conductivity. This increase in conductivity was attributed to

the creation of oxygen vacancies associated with the substitution of phosphorous onto the B-site with tetrahedral coordination, compared to the manganese octahedral coordination, thus leading to the reduction of some Mn^{4+} to give mixed valence Mn^{3+}/Mn^{4+} (26).

This work was also extended to the common SOFC/SOE materials $Ba_{1-x}Sr_xCo_{0.8}Fe_{0.2}O_{3-\delta}$ (BSCF) and $La_{1-y}Sr_yMnO_{3-\delta,}$ (LSM), demonstrating incorporation of phosphate in both systems, as well as improved properties. (27-28). In addition, phosphate doping was shown to help to improve the long-term stability of the cubic form of BSCF at intermediate temperatures ensuring negligible change in conductivity over time. There are, however, some issues with these materials; BSCF exhibits a high thermal expansion coefficient and is high cost (due to the large Co content), while LSM suffers from poor ionic conductivity. Therefore, alternative electrode materials are still being sought.

Herein, we examine the use of phosphate doping of the mixed perovskite Mn/Fe system, $Sr_2MnFeO_{6-\delta,}$ which would represent a novel low-cost cathode material. (29-31). Previous work by Smith et al. showed a related silicon doping strategy was successful in synthesising $Sr_2MnFe_{1-x}Si_xO_{6-\delta}$ with the formation of a single-phase cubic perovskite structure (32). The conductivity was shown to be improved with low levels of Si doping (≤ 0.1), with a decrease at higher silicate levels. We report here that P can also be successfully incorporated into these $(Sr)_2MnFeO_{6-\delta}$ systems and show that the conductivities are higher than the previously reported silicon doped variants.

Experimental

High purity $SrCO_{3,}$ $MnO_{2,}$ $Fe_2O_{3,}$ and $(NH_4)H_2PO_4$ were used to prepare $Sr_2MnFe_{1-x}P_xO_{6-\delta}$ materials. Stoichiometric calculated mixtures of the powders were intimately ground and initially heated to 1000 °C (10 °C min^{-1}) for 12 hours. Samples were then reground and heated to 1250 °C (y=2) for 24 hours with an intermediate regrind. To ensure maximum oxygen content, the resulting samples were held at 350 °C for 12 hours in air.

Powder X-Ray diffraction data were collected in order to determine lattice parameters and phase purity of samples. Data were collected on a Panalytical Empyrean diffractometer equipped with Pixcel 2D detector (Cu Kα radiation). The GSAS-II suite of programs was used to determine unit cell parameters (33).

Samples were analysed to determine transition metal oxidation states using thermogravimetric analysis (Netzch STA 449 F2 Jupiter Thermal Analyser). Samples were heated to 1200 °C (10 °C / min) in N_2 and held at this temperature for 30 minutes to reduce the iron and manganese oxidation states to +3, thus allowing the oxygen content and average metal oxidation to be determined.

^{57}Fe Mössbauer spectroscopy was carried out at 298 K in constant acceleration mode using approximately 25mCi Co/Rh source.

SEM images were collected on a Hitachi Tabletop Microscope TM4000Plus with EDS Oxford Instruments MICSF+ X-stream-2-attachment. The materials were analysed using an

energy-dispersive X-ray spectroscopy to determine the elemental distribution of the phosphate across the sample.

Pellets for conductivity measurements were prepared by ball-milling (350 rpm for 30 minutes) before compacting the material and sintering at the synthesis temperature for 12 hours. Four Pt electrodes were attached with Pt paste and the samples were heated to 950 °C (1 ºC min^{-1}) for 1 hour in air to ensure good contact. Samples were then cooled to 350 °C and held at this temperature for 12 hours to ensure the maximum oxygen content. Conductivities were then measured in air with varying temperatures (400 to 800 °C) using the four-probe dc method.

Results and Discussion

Structural Determination

Previously, Smith et al showed that undoped $Sr_2MnFeO_{6-\delta}$ formed a cubic perovskite, which was confirmed in this study, Figure 1 (32).

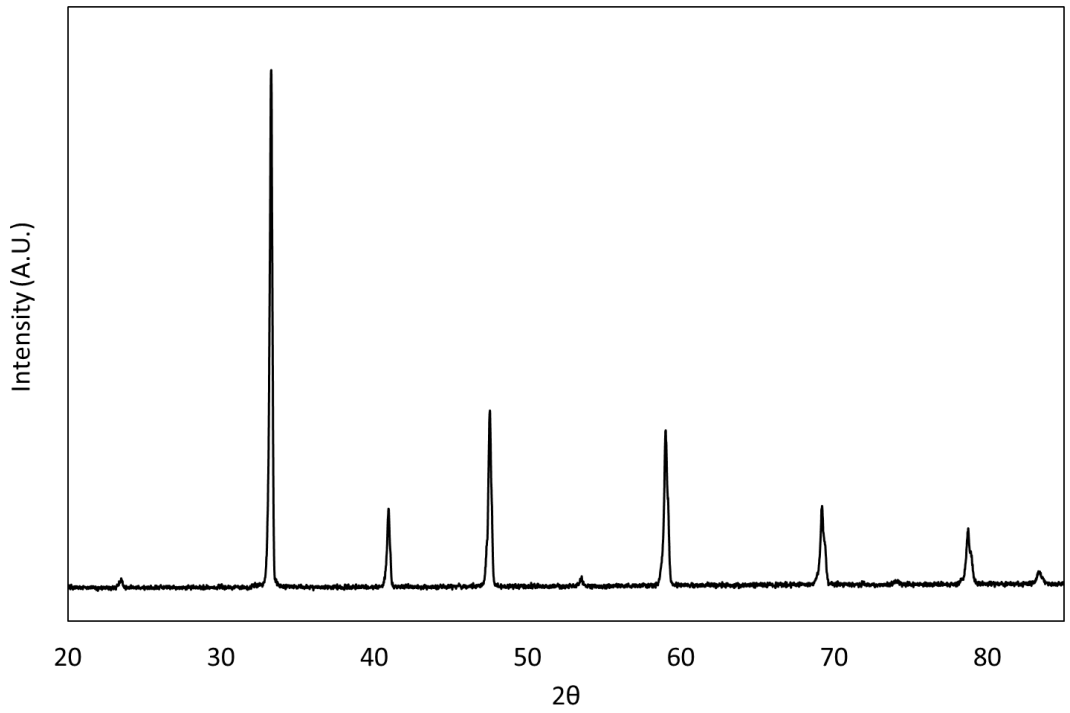

Figure 1. Powder X-ray diffraction data of $Sr_2MnFeO_{6-\delta}$ showing formation of a single phase cubic perovskite.

Powder X-ray diffraction collected on $Sr_2MnFe_{1-x}P_xO_{6\,\delta}$ materials for x = 0.05, 0.10, 0.15, and 0.20 indicated that a cubic perovskite phase was also obtained (Figure 2). However, with increased phosphate content, a small $Sr_3(PO_4)_2$ impurity appears, suggesting the phosphate solubility limit was exceeded for x>0.05.

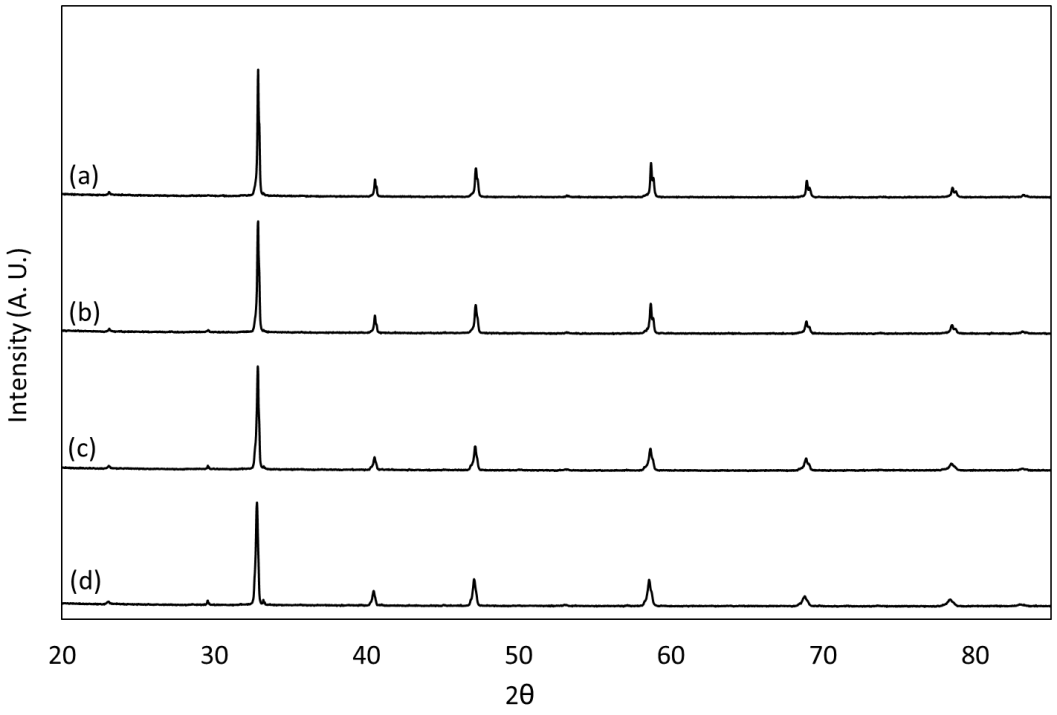

Figure 2. Powder X-ray diffraction from top to bottom: (a) $Sr_2MnFe_{0.95}P_{0.05}O_{6-\delta}$, (b) $Sr_2MnFe_{0.90}P_{0.10}O_{6-\delta}$, (c) $Sr_2MnFe_{0.85}P_{0.15}O_{6-\delta}$, (d) $Sr_2MnFe_{0.80}P_{0.20}O_{6-\delta}$, showing formation of cubic perovskites. Impurity peaks, associated with $Sr_3(PO_4)_2$ can be seen increasing with phosphate doping at around 29º and 32º for x>0.05.

An equivalent Fe deficient sample, $Sr_2MnFe_{0.8}O_{6-\delta}$ without phosphate addition, was synthesised to add further support for the successful incorporation of phosphate. As with other materials discussed, the X-ray diffraction pattern for $Sr_2MnFe_{0.8}O_{6-\delta}$ shows there were multiple phases obtained, Figure 3.

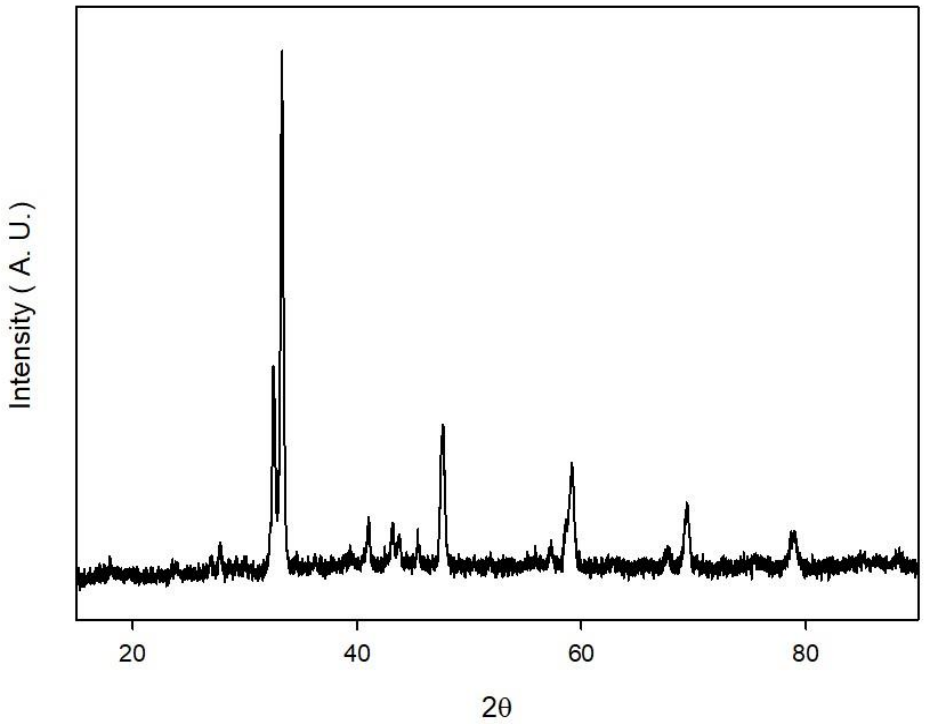

Figure 3. Powder X-ray diffraction of $Sr_2MnFe_{0.8}O_{6-\delta}$ illustrating that without phosphate addition, multiple impurities are seen.

Thermogravimetric analysis was undertaken to measure the mass loss of the material under N_2, and so calculate the oxygen content and the average Mn/Fe oxidation states for the $Sr_2MnFe_{1-x}P_xO_{6-\delta}$ series, Table I.

TABLE I. Oxygen deficiency (δ) and average B-site Metal oxidation state for $Sr_2MnFe_{1-x}P_xO_{6-\delta}$ determined from TGA data.

x	**% Mass Loss**	**δ Value**	**Average B-site Metal Oxidation State**
0.00	2.22	0.48	3.52
0.05	1.55	0.59	3.37
0.10	1.33	0.59	3.33
0.15	1.20	0.57	3.30
0.20	0.38	0.71	3.10

On increased doping with phosphate, an increase in oxygen vacancies is observed, along with a reduction in average Mn/Fe oxidation state. The Mn/Fe site oxidation state was shown to be lower than reported previously for Si doped materials.[32]

^{57}Fe Mössbauer data were collected for the x=0 and 0.05 samples to gain further information on the Fe environment. Chemical isomer shifts δ ≈ -0.23, 0.22/0.23 and 0.31/0.36 mm s^{-1} (Fe/ $Fe_{0.95}P_{0.05}$) can be assigned to Fe^{5+}, Fe^{4+} and Fe^{3+} respectively (Figure 4 and Table II). The measurements confirmed the increase in Fe^{3+} content on doping of phosphate, which correlates with the TGA results.

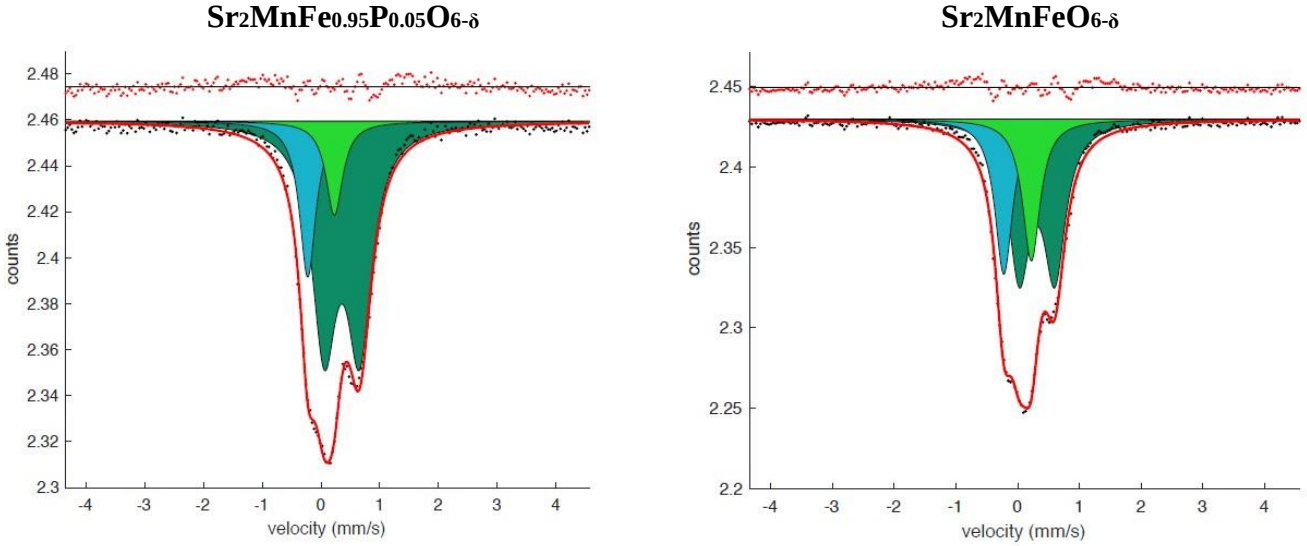

Figure 4. ^{57}Fe Mössbauer spectra for $Sr_2MnFe_{0.95}P_{0.05}O_{6-\delta}$ and $Sr_2MnFeO_{6-\delta}$ at 298 K

TABLE II. ^{57}Fe Mössbauer Spectroscopy data for $Sr_2MnFeO_{6-\delta}$ and $Sr_2MnFe_{0.95}P_{0.05}O_{6-\delta}$

Compound	Assignment	δ ± 0.02 (mms^{-1})	Δ ± 0.08 (mms^{-1})	Area ± 5% (%)
$Sr_2MnFeO_{6-\delta}$	Fe^{3+}	0.31	0.57	55
	Fe^{4+}	0.22	---	23
	Fe^{5+}	-0.23	---	21
$Sr_2MnFe_{0.95}P_{0.05}O_{6-\delta}$	Fe^{3+}	0.36	0.60	72
	Fe^{4+}	0.23	---	11
	Fe^{5+}	-0.23	---	17

Rietveld refinement was performed using the GSAS-II suite of programs based on the space group *P m -3 m* perovskite model using the collected powder X-ray diffraction data for the phosphate doped phases. The unit cell parameters from the refinements are shown in Table III.

TABLE III. Cell parameters and goodness of fit values for $Sr_2MnFe_{1-x}P_xO_{6-\delta}$

X	**a (Å)**	**$_w$Rp**	**Rp**	**χ^2**
0.00	3.8452(7)	3.44	2.55	2.13
0.05	3.8490(3)	3.13	1.51	2.06
0.10	3.8510(8)	4.08	1.52	2.69
0.15	3.8541(3)	3.27	1.55	2.11
0.20	3.8573(1)	3.17	1.51	2.10

The lattice parameters were found to show a small increase with incorporation of phosphate. This observed increase in volume may be attributed to the increase in larger Fe^{3+}/Mn^{3+} ions upon doping with phosphate (as confirmed by ^{57}Fe Mössbauer Spectroscopy), which outweighs any decrease expected from the incorporation of the smaller P dopant.

The elemental distribution of phosphorus across the samples was analysed using SEM-EDX. The $Sr_2FeMn_{0.95}P_{0.05}O_{5.41}$ shows a uniform distribution of phosphorous (thus phosphate) within the material, whereas $Sr_2MnFe_{0.80}P_{0.20}O_{5.29}$ showed regions of rich deposits of phosphorus within the material, emphasising that an impurity phase is present within higher phosphate doped systems, Figure 5.

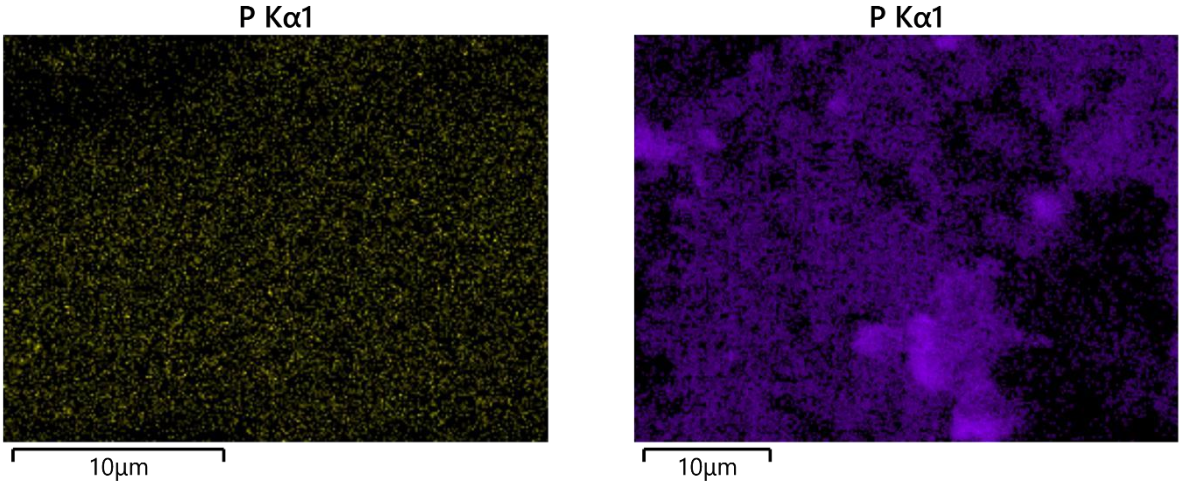

Figure 5: Energy-dispersive X-ray spectroscopy imaging of P (Kα1) content (left) $Sr_2MnFe_{0.95}P_{0.05}O_{5.41}$ and (right) $Sr_2MnFe_{0.80}P_{0.20}O_{5.29}$

Conductivity Measurements

Conductivity measurements of the phosphate doped materials in air are shown in Figure 6.

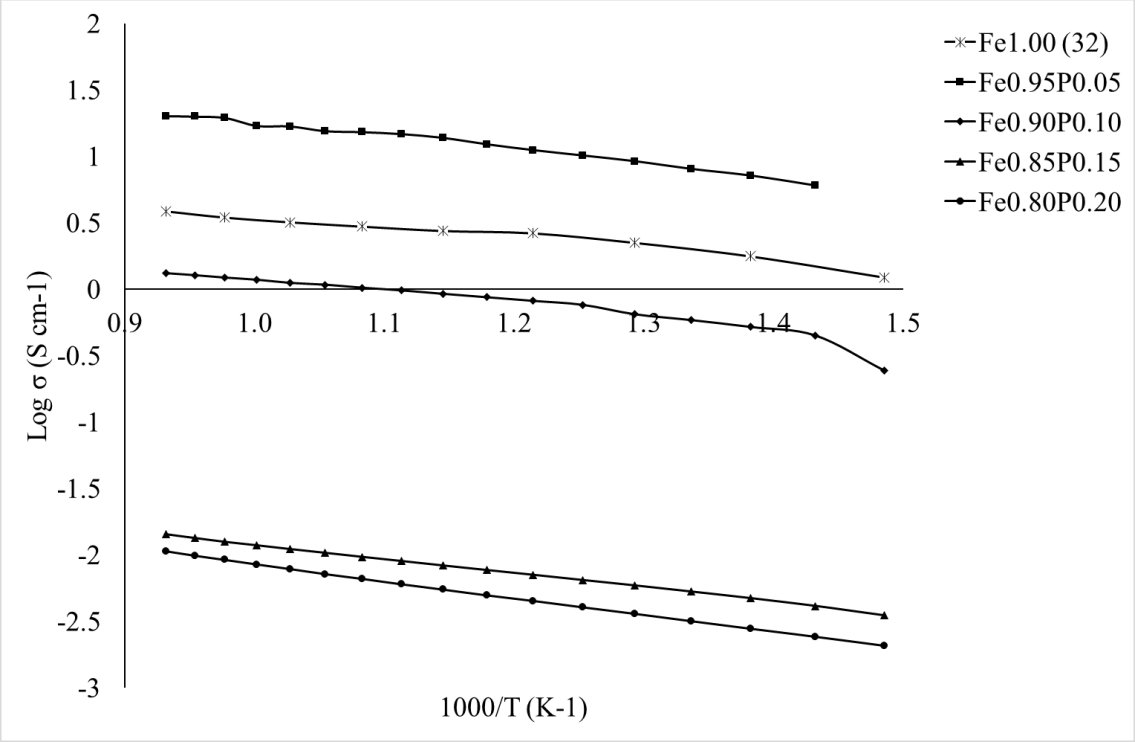

Figure 6: Plot of log σ versus 1000/T for $Sr_2MnFe_{1-x}P_xO_{6-\delta}$

The results highlight that the incorporation of phosphate at low levels (x = 0.05) improves the conductivity significantly before it subsequently reduces at higher phosphate contents. This reduction is attributed to presence of $Sr_3(PO4)_2$ impurities as the solubility limit is exceeded. Overall, the conductivities of the $Sr_2MnFe_{0.95}P_{0.05}O_{5.41}$were higher than the undoped and silicate perovskite structure reported by Smith et al, Table IV (32).

Table IV. Total conductivity data for $Sr_2MnFe_{1-x}(P,Si)_xO_{6-\delta}$ in air.

Compound	Conductivity (S cm^{-1})	Ref
$Sr_2MnFeO_{6-\delta}$	3.19	(32)
$Sr_2MnFe_{0.90}Si_{0.10}O_{6-\delta}$	10.26	(32)
$Sr_2MnFe_{0.95}P_{0.05}O_{6-\delta}$	16.84	This Work

Whilst the electronic conductivity values are generally lower than other SOFC cathode candidates, doping with low levels of other transition metals, e.g Co, may lead to further enhancement.

Conclusions

In this work we have shown that low levels of phosphate can be incorporated into $Sr_2MnFeO_{6-\delta}$. Thermogravimetric analysis was used to calculate the oxidation states of the Bsite metals and found that the $Sr_2MnFe_{0.95}P_{0.05}O_{5.41}$ material had an average Mn/Fe oxidation state of 3.37, lower than previously reported for silicon doping. ^{57}Fe Mössbauer Spectroscopy studies indicated that the amount of Fe^{3+} increased on phosphate doping, in agreement with the TGA data.

Conductivity measurements showed there was a general improvement for $Sr_2MnFeO_{6\delta}$ materials on low level of phosphate incorporation, with a decrease at higher phosphate levels attributed to the presence of impurities as the P solubility limit was exceeded. The conductivities are superior to that of silicon doping and so have potential for Solid Oxide Fuel Cell / Electrolysers applications, as well as potential interest as AFC catalysts.

Acknowledgements

The authors would like to thank the EPSRC for funding (EP/R023662/1; The JUICED Hub [Joint University Industry Consortium for Energy (Materials) and Devices Hub]). The raw datasets associated with the results shown in this paper are available from the University of Birmingham archive https://doi.org/10.25500/edata.bham.00000657. Financial support from the Spanish Agencia Estatal de Investigación under project RTI2018-095303-B-C51 is also gratefully acknowledged.

References

1. A. J. Jacobson, *Chem. Mat.,* **22,** 660-674 (2010).
2. C. Sun, R. Hui and J. Roller, *J. Solid. Stat. Electrochem.*, **22** 2329-2338 (2018).
3. N. Mahato, A. Banerjee, A Gupta, S Ormar and K Balani, *Prog. Mater. Sci.,* **72,** 141-337 (2015).
4. A. Orera and P. R. Slater, *Chem. Mat.,* **22**, 675-690 (2010).
5. J. B. Goodenough, *Phys. Rev.,* **100**(2) 564-573 (1955).
6. O. Chmaissem, B Dabrowki, S Kolesnik, J Maris, J.D. Jorgensen, S. Short, *Phys. Rev.,* **67**(9) 13 (2003).
7. G Corbel, S Mestiri, P. Lacorre, *Solid. State. Sci.,* **7**(10), 1216-1224 (2005).
8. L Suescun, O Chmaissem, J Mais, B Dabrowski, J Jorgensen, *J. Solid. State. Chem.,* **180**(5) 1698-1707 (2007).
9. P. S. Casey, D. Barker, M. A. Hayward, *J. Solid. State. Chem.*, **179**(5) 1375-1382 (2006).
10. C. A. Hancock, J. M Porras-Vazquez, P. J. Keenan and P. R. Slater *Dalton Trans.*, **44**, 10559-10569 (2015).

11. A. Maignan, D. Pelloquin, S. Malo, C. Michel, M. Hervieu and B. Raveau, *Physica C,* **249**(3) 220-233 (1995).
12. C. Greaves and P.R. Slater, *Physica C,* **175**(1), 172-178 (1991).
13. C. Greaves and P.R. Slater, *J. Mater. Chem.,* **1**, 17-21 (1991).
14. M. A. Uribe Laverde, D.A. Landlnez Téllez and J. Roa-Rojas, *Mod. Phys. Lett. B.* **23**(6) 807-813 (2009).
15. P. R. Slater, C. Greaves, M. Slaski and C. M. Muirhead, *Physica C,* **208**(1-2) 193-196 (1993).
16. A. Jarvis, F. J. Berry, J. F. Marco and P. R. Slater. *ECS Trans,* **91**(1), 1467-1476 (2019).
17. J. Deakin, I. Trussov, A. Gibbs, E. Kendrick and P. R. Slater, *Dalton. Trans.,* **47**(37) 12901-12906 (2018).
18. A. Jarvis and P.R. Slater, *Crystals,* **7**(6) 169 (2017).
19. J. M. Porras-Vazquez, R. I. Smith and P. R. Slater, *J. Solid. State. Chem.,* **213,** 132-137 (2014).
20. J. M. Porras-Vazquez, T. Pike, C. A. Hancock, J. F. Marco, F. J. Berry and P. R. Slater, *J. Mat. Chem. A.*, **1**(38) 11834-11841 (2013).
21. J. M Porras-Vazquez, E. R. Losilla, P. J. Keenan, C. A. Hancock, T. F. Kemp, J.V Hanna and P. R. Slater, *Dalton Trans.,* **42**(15) 5421-5429 (2013).
22. C. A. Hancock and P.R Slater, *Dalton Trans.,* **40**(20) 5599-5603 (2011).
23. Y.Pan, X. Xu, Y.Zhong, L.Ge, Y.Chen, J-P M Veder, D.Guan, R O'Hayre, M.Li, G.Wang, H.Wang, W.Zhou, Z.Shao, *Nat Commun,* **11,** 2002 (2020).
24. J. F Shin, K. Joubel, D. C. Apperley and P. R. Slater *Dalton Trans.,* **41**(1), 261-266 (2012).
25. C. A. Hancock, R. C. T. Slade, J. R. Varcoe and P. R. Slater, *J. Solid. State. Chem.* **184**(11), 2972-2977 (2011).
26. J. M Porras-Vazquez, T.F. Kemp, J. V. Hanna and P. R. Slater *J. Mat. Chem.,* **22**(17) 8287-8293 (2012).
27. J. M Porras-Vazquez and P. R. Slater *J. Power. Sources.,* **209**, 180-183 (2012).
28. J. M Porras-Vazquez and P. R. Slater, *Fuel. Cells.,* **12**(6) 1056-1063 (2012).
29. R. V Coates and J. W. McMillan, *J. Appl. Chem,* **14**, 346, (1964).
30. F. Ramezanipour, J. E. Greedan, L. M. D. Cranswick, V. O. Garlea, R. L. Donaberger and J. Siewenie, *J. Am. Chem. Soc.,* **134** 3215-3227 (2012).
31. Y Nakahara, S. Kato, M. Sugai, Y. Ohshima and K. Makino, *Mater Lett.,* **30,** 163-167 (1997).
32. A. D. Smith, M. S. James and P. R. Slater, *ECS Trans,* **91**(1), 1425-1436 (2019).
33. B. H. Toby, R. B. Von Dreele, *J. Appl. Chem,* **46**(2), 544-549 (2013).